PAPER

B-site modified photoferroic Cr³⁺-doped barium titanate nanoparticles: microwave-assisted hydrothermal synthesis, photocatalytic and electrochemical properties†

I. C. Amaechi, [ID] [a] G. Kolhatkar, [ID] [a] A. Hadj Youssef, [a] D. Rawach, [ID] [b] S. Sun [ID] [a] and A. Ruediger*[a]

We report on the synthesis of photoferroic Cr³⁺-doped BaTiO₃ nanoparticles with nominal Cr content ranging from 2–8 mol% by a microwave-assisted hydrothermal method. The absorption properties of the doped systems are significantly enhanced due to the d–d band transition of $Cr^{3+/4+}$. The structural properties of the materials are examined on the basis of lattice distortions given by the tolerance factor and microstrain. Raman scattering provides complementary information on the lattice vibrations indicating a softening of the longitudinal optic (LO) phonon mode located at 716 cm⁻¹ with increasing Cr concentration. The charge transport properties investigated through electrochemical impedance spectroscopy (EIS) demonstrate that there is a reduction in the charge transfer resistance from 5.2 Ω to 4.3 Ω for the undoped and 4 mol% Cr³⁺-doped respectively, which favors the degradation kinetics. The photo-oxidation ability of the systems is evaluated by time evolution of photodegradation of methyl orange under standardized solar irradiation. The experimental results confirm that the best photocatalytic performance is achieved with the 4 mol% Cr³⁺-doped BaTiO₃ nanoparticles, which is ~2.7 times higher than for the undoped sample. Evidence of superoxide radical being the dominant active species is provided by *in situ* reactive oxide species (ROS) capture experiments.

1 Introduction

Due to the increasing world population and industrialization, water pollution has become a major global challenge that has yet to be addressed. The classical solution to this challenge has shown that various physicochemical treatment techniques *e.g.* adsorption and membrane filtration have been effectively deployed but the production of sludge and lack of selectivity for target pollutants limit their applications.[1] On the other hand, wastewater treatment by means of chemical oxidation is also viable mostly through the advance oxidation processes. Unfortunately, the huge energy consumption alongside catalyst recovery have retarded its applicability.[2] Photocatalysis for the decomposition of pollutants has been identified as a promising solution to parts of this challenge. The principle idea consists of employing a semiconducting material to accelerate a photoreaction. Cascades of radicals are generated, leading to photo-

oxidation/reduction of the pollutants. Although experimental results are promising, the elimination of water pollutants through photocatalysis remains limited by poor light absorption, charge carrier separation and transport[3,4] and redox potential of charge carriers on the surface.[5] To address the issue of poor light absorption, both non-metal and metal doping can be employed to improve the light-absorption-improved photocatalytic activities.[6–9] In addition, oxides, such as bimetallic oxides have been identified as promising candidates for such applications. In particular, inorganic oxide perovskites of the type ABO₃ display a high potential for photocatalysis due to their high stability and chemical resistance in aqueous solution.[10] In these materials, A- and B-site are mostly composed of alkaline-earth and transition metals respectively. These materials already find numerous applications as high-temperature (high-T_C) superconductors, piezoelectric and ferroelectric materials, magnetoresistors, multiferroic and catalytic materials *etc.*[11,12] Among the most commonly used oxide perovskites is barium titanate (BaTiO₃). Though conventional TiO₂ has gained wide acceptance, the low absorption cross-section, low adsorption capacity for hydrophobic contaminants, poor charge carrier separation resulting to low quantum yield among others, have placed a limitation on TiO₂-based photocatalysis. To overcome the shortcomings particularly the poor charge carrier

ᵃInstitut National de la Recherche Scientifique, Centre Énergie, Matériaux, Télécommunications (INRS-EMT), 1650 Boulevard Lionel-Boulet, Varennes, Québec J3X 1S2, Canada. E-mail: ruediger@emt.inrs.ca

ᵇDépartement de Chimie, Faculté des Sciences, Université de Sherbrooke, 2500 Boulevard de l'Université, Sherbrooke, Québec J1K 2R1, Canada

† Electronic supplementary information (ESI) available. See DOI: 10.1039/c9ra03439k

separation, the use of piezoelectric materials such as $BaTiO_3$ plays remarkably non-trivial role in improving the photoactivity. In mostly the low symmetry crystal phase, it offers the advantage of increasing the lifetime of charge carriers sufficiently long enough before the recombination that happens on a time scale of picoseconds sets in. $BaTiO_3$ is known to exist in different structural phases as a function of temperature, size and dopants. The high-temperature paraelectric phase shows no spontaneous electric polarization due to Ti-atom occupying the centrosymmetric sites with respect to oxygen[13] while the orthorhombic ($Amm2$, <0–5 °C), rhombohedral ($R3m$, <−80 °C), tetragonal ($P4mm$, <120 °C)[14,15] and high temperature hexagonal ($P4/mmm$, 1460 °C) phases[16] exhibit a ferroelectric response. Ferroelectrics, being non-centrosymmetric, present the bulk photovoltaic effect (BVPE), which significantly contributes to enhanced photoactivity. The BVPE is a second order optical response that can be described by a third rank tensor, $\beta_{ijk} = \dfrac{e l_0 \xi \phi}{\hbar \omega}$, where e, l_0, ξ and ϕ are the electronic charge, mean free path of charge carriers, excitation asymmetry and quantum yield respectively, and the denominator corresponds to the photonic energy.[17] As a hot carrier effect, this bulk property engenders carrier separation and energy loss in form of heat is drastically reduced. This internal electric field-driven separation of charges significantly increases the lifetime, allowing a larger fraction of the carriers to participate in redox reaction thereby enhancing the photoactivity.

However, the photocatalytic activity of $BaTiO_3$ remains limited by low intrinsic absorption. The absorption property can be improved by introducing a dopant in the crystal structure. The doping element is incorporated through atomic substitution of an A- and/or B-site. It is to be chosen carefully depending on the application as it could lead to tuning of the ferroelectric Curie temperature[18] or control of material's permittivity.[19] Furthermore, a difference between radii of the dopant and that of the substituted atom can induce strain in the material that in turn may result in a phase change.[20] In this context, doped $BaTiO_3$ using donor and/or acceptor atoms for environmental remediation has been reported.[6,21,22] Chromium is a promising option, as it is a transition metal with the potential of enhancing the optical properties through an increase in the absorption cross-section in the visible region. That is, its charge transfer center is associated with strong absorption in the visible range, beneficial for energy harvesting. Compared to doping with noble metals, chromium is economically feasible and suitable for large-scale production.

Different chemical routes[23] have been established to synthesize $BaTiO_3$. Some require pyrolysis and crystallization of a disordered precursors, which yields poorly crystalized materials.[24] The microwave-assisted hydrothermal (MWHT) method offers the advantage of a rapid synthesis usually in one step by interaction of dielectric molecules in solid or liquid phase with nonionizing microwave radiation. First results confirmed the suitability of this method has been identified for the synthesis of Cr-doped $BaTiO_3$ for photocatalytic applications.[10] However, although the process was rapid, barium titanate crystallized in the paraelectric phase, while a ferroelectric phase such as the tetragonal structure might be far more beneficial due to the existence of the aforementioned BPVE.

Herein, we synthesize Cr^{3+}-doped $BaTiO_3$ by MWHT and demonstrate its potential for photocatalysis. Structural characterizations reveal that the material is indeed in the tetragonal phase. We use hydrogen peroxide, H_2O_2 to scavenge excess protons that are the primary cause of leakage in the ferroelectric bulk and also contribute to surface defects acting as recombination sites. XPS reveals a negligible concentration (below the detection limit) of hexavalent chromium and the presence of its trivalent state, more appropriate for water purification and environmentally less problematic. Moreover, the misconception of band gap narrowing arising from doping is addressed (see ESI, Fig. S1†) as it is generally misinterpreted as a reduction in the fundamental absorption of a material.

2 Experimental details

2.1 Synthesis of Cr^{3+}-doped $BaTiO_3$ nanoparticles

The nanoparticles of Cr^{3+}-doped $BaTiO_3$ are synthesized by MWHT using high purity and analytical grade precursors of titanium oxide (TiO_2 (>99.7%)), barium hydroxide ($Ba(OH)_2 \cdot 8H_2O$ (>98%)), chromium nitrate $Cr(NO_3)_3 \cdot 9H_2O$ (>98%), and hydrogen peroxide (H_2O_2 (30%)) purchased from Sigma-Aldrich Chemicals. The nanoparticles are prepared from a mixture of TiO_2, $Ba(OH)_2 \cdot 8H_2O$ and $Cr(NO_3)_3 \cdot 9H_2O$ in the molar ratio of 18 : 29 : 2 dissolved in distilled water.

A TiO_2 slurry is prepared by dispersing the powder in distilled water. The Ti^{4+} solution is then magnetically stirred for 10 min followed by the addition of $Ba(OH)_2 \cdot 8H_2O$, $Cr(NO_3)_3 \cdot 9H_2O$ (Cr^{3+} = 2, 4, 6 and 8 mol%), and 2 mL of H_2O_2. The H_2O_2 is added to scavenge the excess H^+ ions, which are the main cause of electronic leakage. The resulting mixture is then stirred for another 20 min to obtain a homogeneous solution.

Subsequently, the mixture is transferred into a Microwave Acid Digestion autoclave (Parr Instrument) with 23 mL capacity. The reactor assembly is placed in a Panasonic Inverter Microwave Oven (2.45 GHz) operating at 120 W for 10 min. These parameters correspond to 1 cycle of microwave irradiation. To avoid overpressure, the reactor assembly is allowed to cool down almost to room temperature for ∼1 h before repeating the process of microwave irradiation. Finally, after a total of three cycles, the final product is washed in distilled water, filtered and dried at 80 °C for 15 h. The same procedure is employed to synthesize the undoped $BaTiO_3$ sample but without the addition of chromium.

2.2 Characterization of samples

The phase identification of the samples is done by powder X-ray diffraction (XRD, Bruker D8 Advance) using Cu-K$_\alpha$ radiation (λ = 1.5406 Å). 2θ scans in the 20–60° range are performed with a 0.02° step size. The absorbance spectra are measured in the 300–600 nm range using a (PerkinElmer, Lambda 750) UV-visible-NIR spectrometer with 1 nm spectral resolution. Samples for the optical absorption are prepared by dispersing a weighed quantity of the nanoparticles in distilled water

followed by dip-coating of a pretreated quartz substrate. Also, plain quartz substrate is used as reference. Raman scattering spectra are acquired with a Horiba iHR320 equipped with a 473 nm solid state blue Cobolt 04-01 laser (linearly polarized, TEM00) and a thermoelectrically cooled Horiba Scientific Synapse Back-Illuminated Deep Depletion CCD detector. The bright field surface images of the samples are acquired by transmission electron microscopy (TEM, JOEL Model: JEM-2100F). The chemical composition of the samples is investigated by X-ray photoelectron spectroscopy (XPS) using a VG Escalab 220i XL system equipped with a 1486.6 eV Al-K$_\alpha$ source. The C–C bond of C 1s peak with binding energy of 284.6 eV is used to calibrate the whole spectra.

A reactor assembly consisting of a three-electrode system connected to a Zahner Elektrik Zennium Photoelectrochemical Workstation is employed for the electrochemical measurements. In the three-electrode system *i.e.* counter, reference and working electrode, Pt, Ag/AgCl and photoferroic films on ITO are used, respectively. The cell electrolyte consists of a 0.5 M Na$_2$SO$_4$ solution. The working electrode is prepared by dispersing 50 mg of the photoferroic nanoparticles in 600 μL of a *N*-methyl-2-pyrrolidone (NMP) and polyvinylidene fluoride (PVDF) composite solution. The resulting solution is ultrasonicated for 10 min before being spin-coated on the pretreated ITO substrates at 4500 rpm. Lastly, the spin-coated electrodes are dried in the oven at 100 °C for 15 h.

2.3 Photocatalytic activity measurements

The photocatalytic degradation of methyl orange with Cr^{3+}-doped BaTiO$_3$ nanoparticles is carried out in a photochemical reactor using a calibrated solar simulator equipped with a 150 W xenon (Xe) lamp (Model-#SS50AAA, PET Photoemission Tech., Inc.). The setup is as illustrated in Fig. 1. The light intensity from the solar simulator is adjusted to 100 mW cm^{-2}. In a typical test, 50 mg of the as-synthesized nanoparticles are dispersed in 50 mL of 20 mg L^{-1} methyl orange solution. The dispersed nanoparticles are magnetically stirred in the dark for 30 min in order to achieve adsorption–desorption equilibrium. The quartz photochemical reactor is placed under continuous stirring and illumination during the experiments. The residual concentration C_t of the dye molecules is determined by evaluating the photovoltage response from a photodetector placed directly behind the reactor. For consistency and reproducibility, the position of the photodetector remains unchanged throughout the

Fig. 1 Schematic of the set-up employed for the photocatalytic activity measurements.

experiment. The absorbance can be obtained from a logarithmic ratio of the photovoltages V_0 and V_t, where V_0 and V_t are the photovoltage responses at initial (C_0) and residual (C_t) concentration, respectively.

The role of different active species in the photocatalytic degradation of methyl orange with Cr^{3+}-doped BaTiO$_3$ nanoparticles are verified by investigating the effect of adding the following scavengers: benzoquinone (BQ), *tert*-butyl alcohol (TBA), and ethylene diaminetetraacetic acid (EDTA). Under similar experimental condition outlined, 0.5 mM BQ, 2 mM TBA, and 2 mM EDTA are introduced differently into a 50 mL capacity photochemical reactor to scavenge the following radicals; O$_2^{-\bullet}$, h$^+$, and OH$^\bullet$ respectively.

3 Results and discussion

3.1 Structural analysis

The structural properties of the samples are identified using XRD. Fig. 2a shows the XRD patterns of the as-synthesized samples with different chromium contents. The patterns show diffraction peaks that correspond to tetragonal BaTiO$_3$ of *P4mm* space group (JCPDS # 01-075-1606).[14,22] All the patterns present a secondary phase corresponding to BaCO$_3$, in agreement with literature.[14,25] One possible source of this phase comes from the high surface reactivity of BaTiO$_3$ nanoparticles with dissolved CO$_2$ resulting in carbonate formation. Due to high basicity of BaO, which constitutes 50% of the vicinal (100) surfaces, BaCO$_3$ is formed on the surface of the nanoparticles through the formation of CO$_3^{2-}$ from dissolved CO$_2$ species during synthesis.[26]

While Cr doping may result in the presence of different ions with different radii: Cr^{2+} (0.80 Å), Cr^{3+} (0.615 Å), Cr^{4+} (0.55 Å), Cr^{5+} (0.49 Å) and Cr^{6+} (0.44 Å),[27] the close ionic radii of Cr^{3+} and Ti^{4+} (0.62 Å) make this configuration the most favorable in the system. Since the incorporation of Cr^{3+} occurs through an aliovalent substitution, the charge compensation mechanism induces the formation of oxygen vacancies $V_O^{\bullet\bullet}$. These oxygen vacancies $V_O^{\bullet\bullet}$ being unstable, they get reduced into singly ionized oxygen vacancies $V_O^{\bullet}$ according to $V_O^{\bullet\bullet} + e^- \leftrightarrow V_O^{\bullet}$.[28,29] However, if the number of oxygen vacancies becomes too high, the BaTiO$_3$ tetragonal structure becomes distorted and transforms into the hexagonal configuration. From the XRD patterns, no peak associated with the hexagonal phase is observed. This indicates that the distortion induced by oxygen vacancies can be accommodated by the tetragonal structure, an advantage of Cr doping over Fe, Co or Mn doping.[30,31]

To quantify the stability and degree of distortion of the TiO$_6$/CrO$_6$ octahedra, the Goldschmidt tolerance factor t[32] is calculated according to

$$t = \frac{(R_{Ba} + R_O)}{\sqrt{2}(R_{Ti/Cr} + R_O)} \quad (1)$$

where R_{Ba}, $R_{Ti/Cr}$ and R_O are the ionic radii of Ba^{2+} ion in 12-fold coordination, Ti/Cr^{3+} ion in 6-fold coordination and O^{2-} ion in 6-fold coordination respectively. By considering the ionic radii of Ba^{2+} (R_{Ba} = 1.61 Å) and Ti^{4+}/Cr^{3+}, a tolerance factor of ~0.81 is estimated for all samples. This indicates a distortion of the
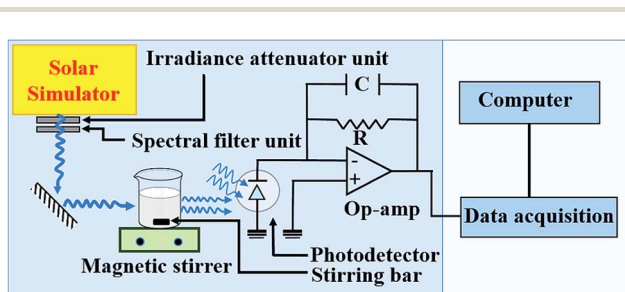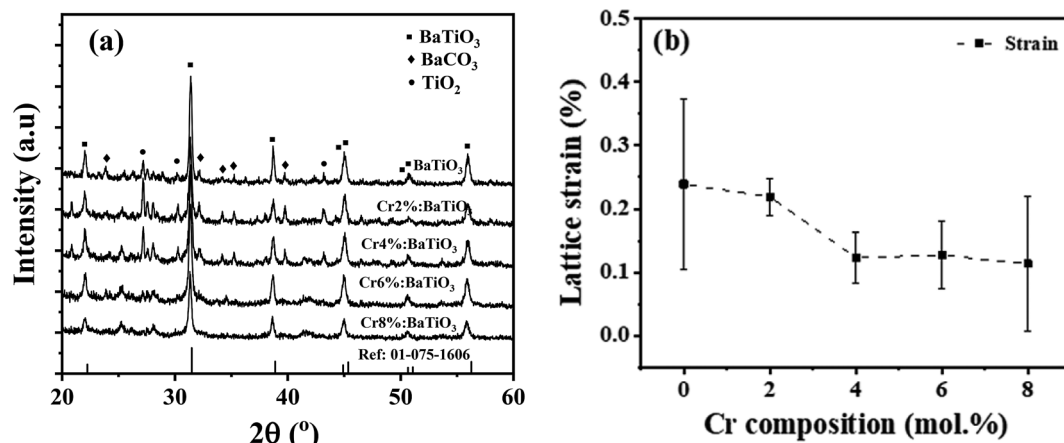
Fig. 2 (a) XRD patterns of undoped and Cr^{3+}-doped $BaTiO_3$ nanoparticles. The peaks reflecting $BaTiO_3$, $BaCO_3$ and TiO_2 are indicated by ■, ◆ and ● respectively. (b) Variation of lattice microstrain as a function Cr composition.

octahedra, as suggested by the splitting of the peak at $2\theta = 45°$ into (200) and (002) for the tetragonal phase.

Moreover, the different ionic radii of chromium and titanium result in strain in the crystal, which is evidenced by a broadening in the diffraction line profile of the host lattice. If this strain is sufficiently large, it can cause a CrO_6/TiO_6 octahedra tilting causing a structural phase transition. To determine the lattice strain, the XRD peaks are fitted with a Gaussian weighting function.[14] The lattice strain ε is determined from[33]

$$\varepsilon = \frac{\beta_{2\theta}}{4 \tan \theta}, \qquad (2)$$

where $\beta_{2\theta}$ and θ are the FWHM of individual diffraction peaks and Bragg's angle, respectively. An average value of ε is obtained for each composition by performing this calculation for all diffraction peaks.

Fig. 2b shows the variation of the mean lattice strain thereby obtained as a function of Cr composition. It shows that the strain decreases monotonically with increasing Cr concentration, from 0.25% in the undoped material, down to ~0.11% in the 8 mol% Cr^{3+}-doped sample. One of the reasons for the observed trend may be likely due to increase in grain size as evidenced from the TEM. The strain may also stem from a shortened Cr–O bond length considering the next unit cell with CrO_6 octahedron. These low values indicate that the strain is not high enough to induce a structural phase transition.[34] Evidence of this tetragonal phase and absence of octahedra tilting is also provided by Raman scattering results.

3.2 Raman spectroscopy

Raman spectroscopy is employed to further study the influence of Cr^{3+} on the lattice vibration and microstructural properties of the materials. The Raman active phonon modes of undoped and Cr^{3+}-doped $BaTiO_3$ nanoparticles with different Cr compositions are shown in Fig. 3a. Multiple Raman peaks are observed in the 0–800 cm^{-1} range at 185 cm^{-1}, 264 cm^{-1}, 310 cm^{-1}, 518 cm^{-1} and 715 cm^{-1}. These peaks corresponds to those reported for the tetragonal phase of $BaTiO_3$.[14,35,36] These

spectra further confirm that the tetragonal phase remains the dominant phase in all samples. The acquired Raman spectra are deconvoluted into a series of Lorentzian-shaped peaks (Fig. S2†) from where the phonon frequency and FWHM of individual peaks are determined. The peaks centered around 185 cm^{-1} and 264 cm^{-1} are attributed to the E(TO) and A1(2TO) mode (stiffened components of the soft mode) respectively; the asymmetric broad peak at ~518 cm^{-1} corresponds to the A1(3TO), E(TO) mode, while the sharp peak at ~310 cm^{-1} and the broad peak at ~715 cm^{-1} are attributed to the B1, E(LO + TO) and A1(LO). E(LO) modes, respectively. While the second order peaks at 270 cm^{-1} and 518 cm^{-1} persist in the cubic phase, the Raman peaks located at 310 cm^{-1} and 715 cm^{-1} are first order modes of the room temperature tetragonal $BaTiO_3$ phase.[13,14,35,37,38] In particular, the 310 cm^{-1} Raman mode represents the torsional vibration of Ti–O_3 when the TiO_6 octahedron undergoes an order-disorder transition.[39]

By comparison of the spectra of the different samples, we observe a significant drop in intensity of 306 cm^{-1} and 713 cm^{-1} Raman peaks as the Cr^{3+} content increases. This suggests a gradual suppression of the tetragonality with increasing doping concentration. The decrease in Raman intensity of the 715 cm^{-1} phonon mode is accompanied by an increase in FWHM of the Raman line shape as shown in Fig. 3b. This indication of a shortened phonon lifetime is generally associated to defect-induced disorder that enhances interference effects between coupled modes.[40,41] The two bands at 268 cm^{-1} and 518 cm^{-1} can still be observed with enhanced peak broadening indicating local Ti^{4+} ion disorder as the Cr^{3+} composition increased in $BaTiO_3$ lattice.[37]

In addition, the presence of residual TiO_2 from the fabrication is indicated by one strong intense peak at low frequency 144 cm^{-1} and two weak peaks at ~396 cm^{-1} and ~639 cm^{-1}. These bands are assigned to the E_g, B_{1g} and E_g modes of anatase TiO_2, respectively.[42] The peak at 226 cm^{-1}, due to in-plane bending vibrations of the CO_3^{2-} ion, denotes the presence of $BaCO_3$ arising from the surface reactivity of CO_2 with $BaTiO_3$ phase[35,43] in agreement with the XRD results. Finally, the
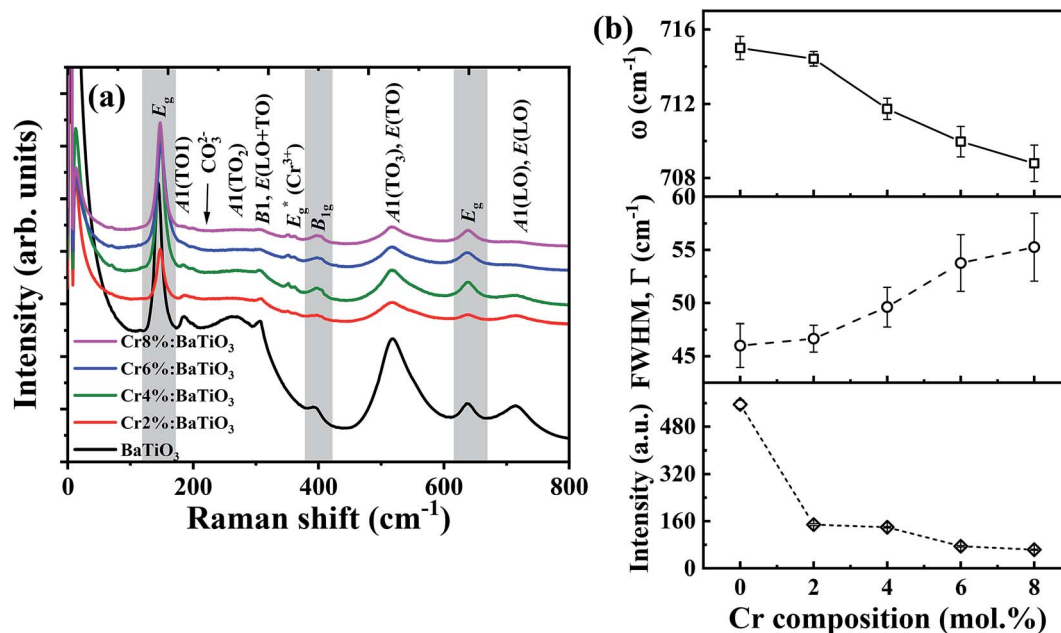
Fig. 3   (a) Raman spectra of undoped and Cr^{3+}-doped $BaTiO_3$ lattice. Areas in ash colour indicate Raman modes of residual TiO_2. (b) Variation of phonon frequency, ω (thick line), FWHM (dash line), and Raman intensity (short-dash line) of 715 cm^{-1} phonon mode with Cr composition. The solid lines are guide to the eye.

phonon frequency at 354 cm^{-1} is due to E_g stretching vibration of Cr–O bonds in the structure.[44,45] This further confirms that Cr^{3+} primarily substituted Ti^{4+} with evidence of local distortion in the vicinity of the CrO_6 octahedron.

3.3   X-ray photoelectron spectroscopy

In order to understand the binding energies associated with the chemical states of different elements present in Cr^{3+}-doped $BaTiO_3$, XPS is performed on the undoped sample and on the 4 mol% Cr-doped $BaTiO_3$. The general survey is shown in Fig. 4a. Peaks associated to Ba, O, Ti and Cr are measured. Ba 4d and Ba 4p peaks are also detected. The high-resolution scans for individual elements are shown in Fig. 4b–e. The most intense peak corresponding to Ba $3d_{5/2}$ is resolved at 778.28 eV and 780.34 eV for the undoped and (777.96 eV and 779.35 eV) for the 4 mol% Cr-doped sample, respectively (Fig. 4b). These peaks are typical of barium ions in the 2+ oxidation state.[46] The addition of dopant causes an energy shift ΔE of 0.32 eV and 0.99 eV to the lower energy state in Ba $3d_{5/2}$ respectively. The O 1s peak (Fig. 4c) is also deconvoluted for proper identification. It is composed of two peaks located at 528.99 eV and 530.61 eV linked to oxygen bonded to $BaTiO_3$ lattice and surface-adsorbed oxygen atoms.[46] Three Gaussian peaks are used to fit the spectrum for the doped sample. The peak at 529.74 eV may likely be a surface adsorbed oxygen bonded to carbon (C–O) due to the presence of carbonate contaminant consistent with the XRD result. The Ti 2p core level showing the $2p_{3/2}$ and $2p_{1/2}$ states are shown in Fig. 4d. In the spectrum, the Ti $2p_{3/2}$ peak is more intense and narrower than the Ti $2p_{1/2}$ peak. The peaks at 457.75 eV and 463.68 eV are binding energies of tetravalent titanium in both states whereas those at 457.58 eV and

463.68 eV correspond to binding energies of reduced titanium (Ti^{3+}) likely initiated by charge compensation mechanism due to defects. The fitted peaks at 457.75 eV and 463.35 eV show a spin–orbit splitting of 5.60 eV which is consistent with the reports of Södergren et al.[47] The addition of Cr impurity increases the splitting orbital energy slightly to 5.78 eV with a blueshift of 0.04 eV and 0.37 eV for both peaks respectively.

Fig. 4e depicts the spectrum of Cr 2p doublet, which is deconvoluted into four different peaks. The most intense peak for the Cr $2p_{3/2}$ and Cr $2p_{1/2}$ core levels at 576.7 eV and 585.9 eV confirms the presence of Cr^{3+} state, whereas those at 575.5 eV and 584.4 eV correspond to the tetravalent oxidation state of chromium.[48,49] The fit results showing low peak area for the Cr^{4+} indicate that it manifests through charge compensation mechanism while the Cr^{3+} state remains the dominant species. In comparison to the Cr $2p_{1/2}$ peak, a splitting orbital energy of 9.20 eV is estimated relative to Cr $2p_{3/2}$. Based on these observations, the possibility of hexavalent metallic Cr (Cr^{6+}) formation is excluded from the doped samples making our Cr^{3+}-doped $BaTiO_3$ more appropriate for wastewater purification. The report is in agreement with the XRD and Raman results.

3.4   TEM and energy dispersive X-ray spectroscopy (EDX)

The particle size distribution and microstructural properties of the Cr^{3+}-doped $BaTiO_3$ nanoparticles are investigated using TEM. Fig. 5a–e show the bright field TEM images of the undoped and Cr^{3+}-doped $BaTiO_3$ nanoparticles. The surface of the undoped sample is composed of partially aggregated, facetted particles with a high shape isotropy. The addition of chromium appears to promote a shape anisotropy towards rods, this however remains to be statistically consolidated. Beyond
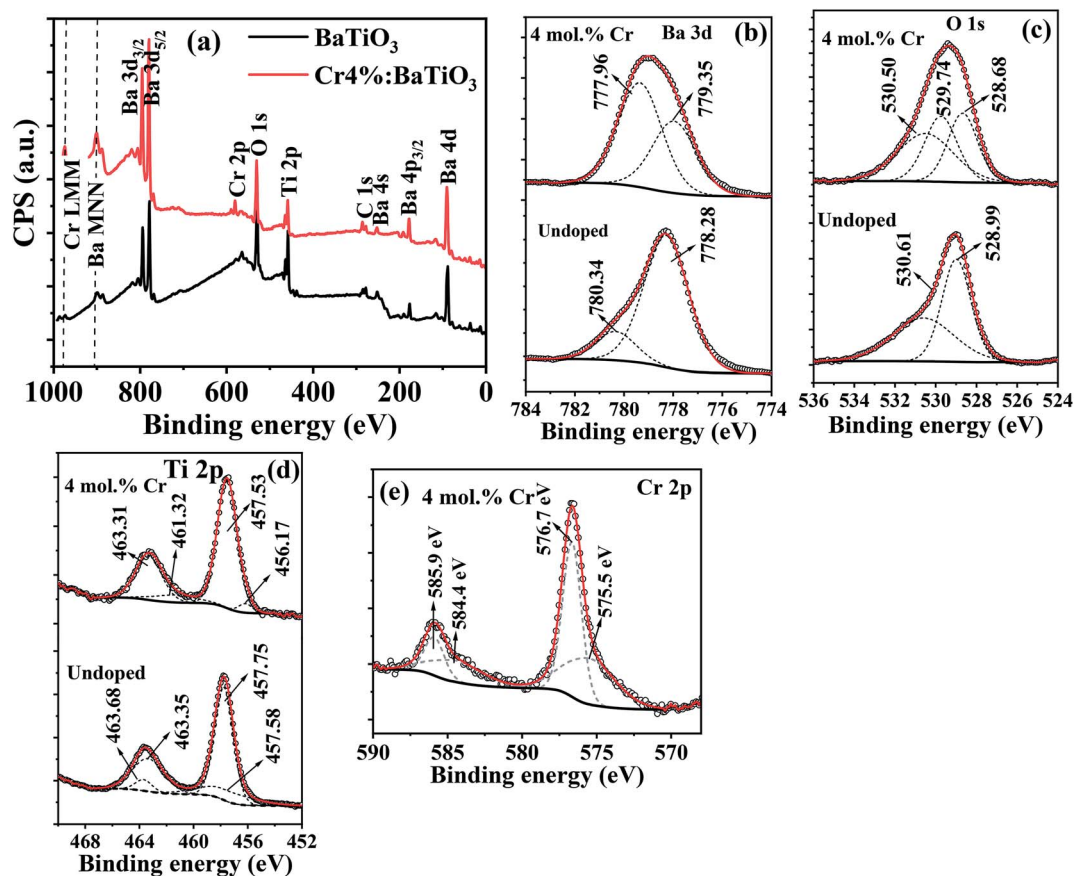
Fig. 4 The XPS (a) survey spectra of undoped and 4 mol% Cr^{3+}-doped $BaTiO_3$ nanoparticles; high resolution scan of (b) Ba 3d (c) O 1s (d) Ti 2p and (e) Cr 2p.

4 mol% Cr concentration, it appears as if individual facets decrease in size, promoting surfaces with higher Miller indices that indicate a weakening of the crystalline bonds. Since the nanograins have different degrees of shape anisotropy, the estimation of the particle size has to take this into consideration. The insets of Fig. 5a–e give an estimate of the particle size distribution deduced from the TEM images. We can see that the particle size increases up to 79 ± 4 nm for the 4 mol% Cr composition before decreasing due to high concentration of chromium. At this point, we would like to point out that due to shape anisotropy of the nanoparticles, it is rather challenging to quantitatively estimate the overall particle size.

The elements present in the undoped and 4 mol% Cr^{3+}-doped $BaTiO_3$ samples are independently identified by energy dispersive X-ray (EDX) spectroscopy. Fig. S3† shows the elemental composition of the samples as analyzed by EDX. The peaks on the energy scale confirm the presence of Ba, Ti, O, and Cr in the system.

3.5 Optical absorption studies

For photocatalytic applications, light utilization is crucial as it determines the numbers of available photogenerated charge carriers that participate in the catalytic redox reaction. The energy band gap is an important intrinsic property

that defines the intrinsic optical absorption of the material. Fig. 6a shows the optical absorption spectra of the samples. The intrinsic absorption is the same for all the samples and can be assigned to charge transfer of valence band electrons to conduction band. In the chromium-doped samples, an additional absorption band appears in the 420–480 nm spectral range. This is due to d–d band transitions between the high spin Cr^{3+} center and Ti^{4+} site resulting in a weak shoulder peak.[50] The light induced excitation of $Cr^{3+/4+}$ exchange-coupled pair is also possible due to multivalent state transitions in chromium.[51] Furthermore, no other absorption was recorded in the far visible region. The apparent absorption threshold is extracted for these curves and presented in Fig. 6b. In the undoped sample, it is estimated to be near 390 nm. Upon the introduction of 2 mol% Cr, it redshifts to 458 nm. When the Cr content is further increased no significant shift is observed and the apparent absorption edge remains in the 458–475 nm range. The extracted cut-off wavelength dependence on Cr content follows a theoretical model as shown by the fit. Hence as long as the lattice is not completely changed and the unit cells remain within the limit of structural modifications, there is always a slight increment in absorption upon doping. Therefore, Cr^{3+} doping offers the possibility of
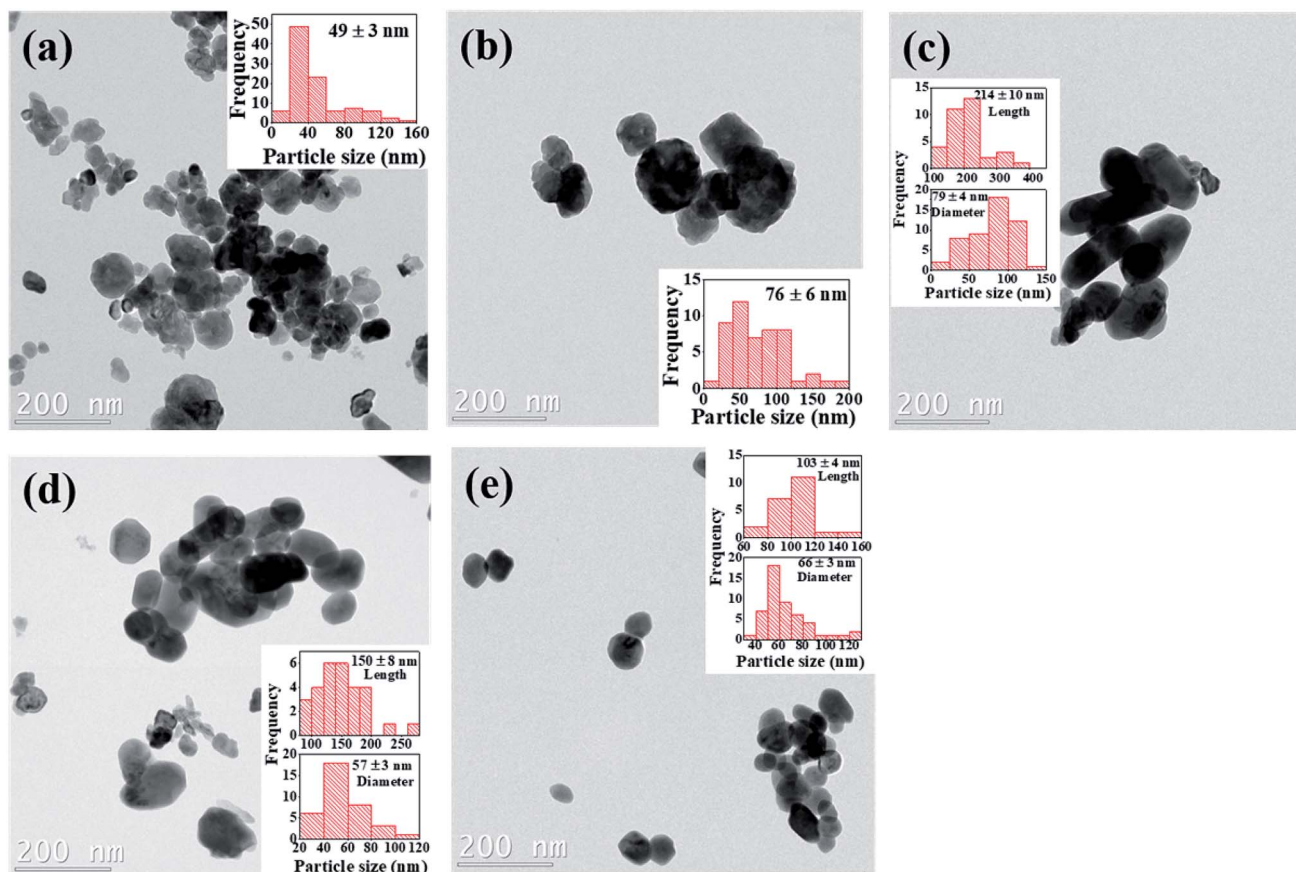
Fig. 5 Bright field TEM images of (a) undoped (b) 2 mol% Cr (c) 4 mol% Cr (d) 6 mol% Cr and (e) 8 mol% Cr^{3+}-doped $BaTiO_3$ nanoparticles; insets are the corresponding particle size distribution.

modulating the light absorption properties as evidenced by the redshift of the absorption edge.

3.6 Photoelectrochemical measurements

The degradation kinetics of a catalytic redox reaction is mainly determined by the charge transfer properties of the material. For this purpose, photoelectrochemical measurements are conducted to gain insight on the process of charge transfer. We examine the electrochemical behavior of the undoped, 4 mol% and 8 mol% Cr. Fig. 7a shows the time dependent photocurrent response of the 4 mol%, 8 mol% and undoped samples measured by chopped light amperometry (CLA) under simulated sunlight. In all the structures, the photocurrent profiles exhibit a photoresponse that decays over time. Also, the
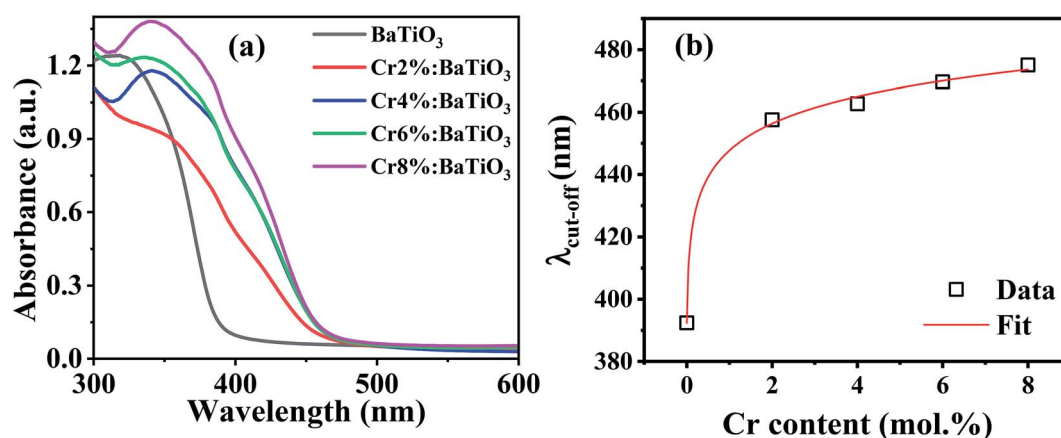

Fig. 6 (a) Optical absorption spectra of the undoped and Cr^{3+}-doped $BaTiO_3$ samples, and (b) variation of apparent cut-off wavelength with Cr composition.
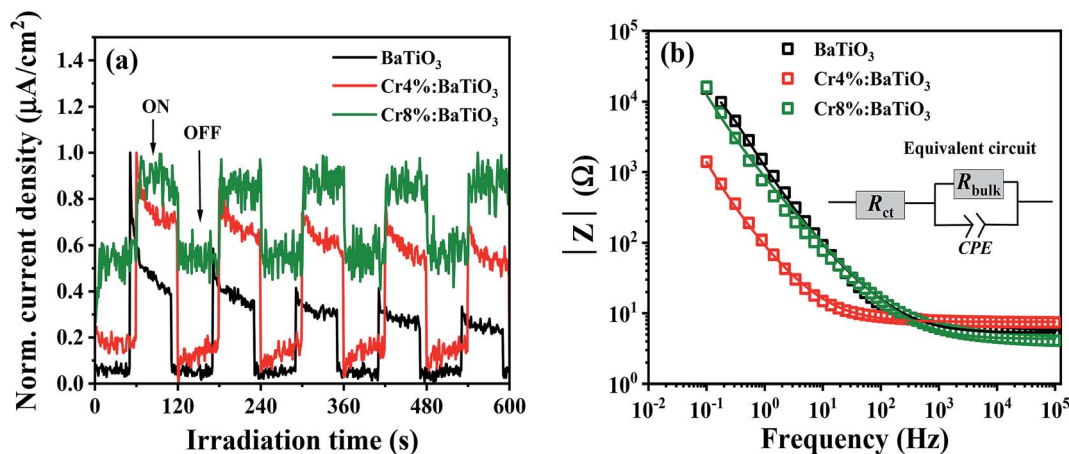
Fig. 7 (a) Normalized photocurrent density recorded at 0 V as a function of the irradiation time. (b) EIS Bode plots of the undoped (black), 4 mol% (red) and 8 mol% (green) Cr^{3+}-doped BaTiO$_3$ samples under light irradiation.

photocurrent density observed under homogenous illumination is low. Such a behavior is typical of ferroelectric crystals and is caused by poor bulk dc conduction, reflecting a low charge carrier mobility.[52]

The electrochemical impedance spectroscopy investigates the interfacial charge transfer properties of the samples under standardized solar light irradiation. The variation of the absolute value of the impedance $|Z|$ with frequency (Bode plots) for the three samples (4%, 8% and undoped) is presented in Fig. 7b. In the low frequency regime, it is observed that the impedance of doped samples decreases in comparison to that of the undoped sample. This feature indicates a low charge transfer resistance of the doped materials in electrolytic solution. Similar observation has been reported by Yu et al.[53] which favors the photoactivity of methyl orange. In order to extract the charge transfer resistance of these materials, a Z view software is used for the complex non-linear least-squares regression. The equivalent circuit comprises of charge transfer resistance (R_{ct}) which is in series with a parallel connection of bulk resistance, (R_{bulk}) and a constant phase element (CPE) as depicted in the inset of Fig. 7b. The electrochemical impedance (R_{ct}) obtained from the regression analysis shows a decrease from $5.2 \pm 0.2 \, \Omega$ to $4.3 \pm 0.03 \, \Omega$ for the samples. This suggests that the kinetics of the electron transfer is faster in the doped nanostructures, an asset for photocatalysis.

3.7 Photocatalytic activity

The photocatalytic performance of photoferroic Cr^{3+}-doped BaTiO$_3$ nanoparticles is evaluated by investigating the photodegradation of methyl orange, a common pollutant.[54] The time dependent adsorption as well as photodegradation of the organic pollutant by undoped and Cr^{3+}-doped BaTiO$_3$ samples with different molar concentrations of Cr in the dark and under simulated light irradiation is shown in Fig. S4† and 8a respectively. From the plot (Fig. S4†), the adsorption capacities show that the 4 mol% Cr doped sample provides an efficient adsorption due to the aspect ratio offered by a composition of geometries as observed in the morphology. The photo-oxidation

of methyl orange under simulated light irradiation without photocatalyst is included as a reference (MO), and does not depict any significant changes over time. This demonstrates that neither photolysis of the methyl orange solution nor contribution of chromium oxide to redox reaction is observed. As photodegradation follows the Beer–Lambert model, all the plots are fitted exponentially. The doped samples show a higher visible light photocatalytic activity than the undoped BaTiO$_3$ due to an enhanced light harvest, as depicted in Fig. 8b. The difference in degradation efficiency between the undoped and doped materials could be due either to the higher absorption cross-section offered by Cr^{3+} doping, or to the BPVE. Since, the absorption cross-section is extended by a few tens of nanometer, the dominant factor responsible for this increase is attributed to BPVE driven enhanced charge carrier separation. After 90 min of visible light irradiation, the photodegradation efficiency of methyl orange is 52% for undoped BaTiO$_3$ while 72, 87, 80 and 77% are observed for the 2 mol% Cr, 4 mol% Cr, 6 mol% Cr and 8 mol% Cr, respectively. The best photocatalytic performance is therefore achieved with the 4 mol% Cr-doped BaTiO$_3$ and compares well with degradation efficiencies reported in literature (Table S1†). In particular, the presence of asymmetric velocities of charge carriers in the potential of these tetragonal materials makes the difference when compared to the same material for catalytic reduction of nitrobenzene to aniline with a yield of 98.2% in 6 h (i.e. 63.4%, recalculated to 90 min).[10]

Furthermore, the dominant reactive species present during the photocatalytic degradation are explored using BQ, TBA, and EDTA as scavengers for the following radicals; O$_2^{-\bullet}$, h$^+$, and OH$^\bullet$ respectively. With the 4 mol% Cr^{3+}-doped BaTiO$_3$ nanoparticles exhibiting the best photocatalytic performance, the irradiation time-dependent photocatalytic degradation (C_t/C_0) of methyl orange with and without scavengers are investigated and results are displayed in Fig. 8c. It is observed that 43% of the methyl orange is degraded after 90 min when BQ is added to the system. This demonstrates the inhibiting role of BQ in degrading the organic dye in comparison to the efficiency
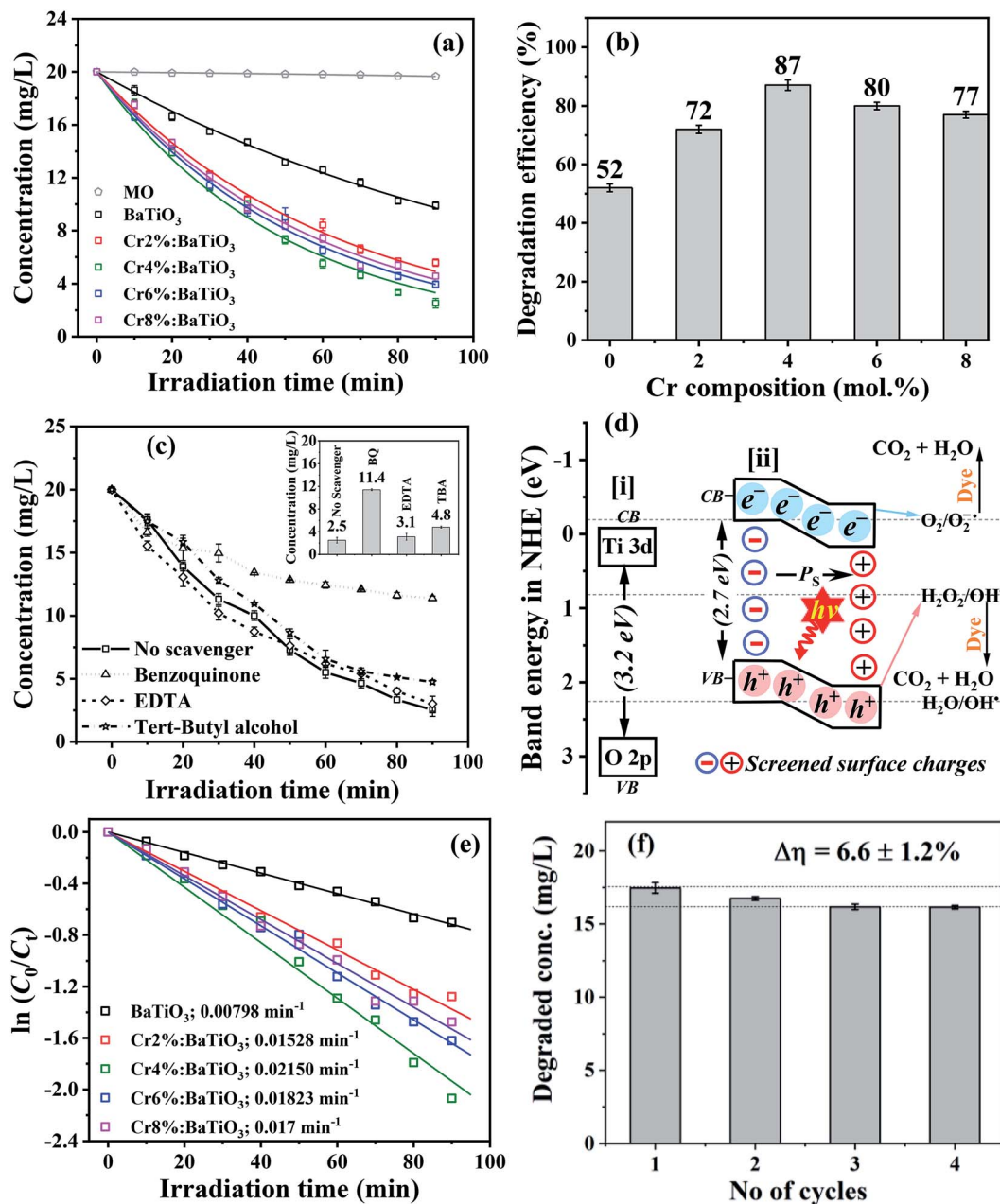
Fig. 8 (a) Irradiation time dependent photodegradation of methyl orange (MO) over undoped and Cr^{3+}-doped $BaTiO_3$ samples. (b) The variation of photodegradation efficiency as a function of Cr composition. (c) The photodegradation of methyl orange over 4 mol% Cr^{3+}-doped $BaTiO_3$ sample with different scavengers. (d) The energy band structure illustrating the charge transfer mechanism in the doped photoferroic. (e) Photodegradation kinetics of the samples. (f) Photostability of 4 mol% Cr^{3+}-doped $BaTiO_3$ after 4 consecutive cycles.

obtained in the absence of the scavenger. When TBA is added, the kinetics slows down slightly, yielding a degradation efficiency of 76% after 90 min. On the other hand, a recovery of degradation time (~2 min) is recorded when EDTA is added to the system. Hence, at 80 min of light exposure, the concentration decreased to 3.9 ± 0.25 mg L^{-1} representing ~80% degradation efficiency. It suggests an enhanced kinetics through a reduced trapping of holes, which would otherwise cause recombination of charge carriers. In general, the results show the dominance of $O_2^{-\bullet}$ in the degradation of methyl

orange when the photoferroic nanoparticles are illuminated. A further account of the photocatalytic degradation pathway being initiated by majorly a reaction between streams of photoelectrons and surface adsorbed oxygen is discussed next.

To better understand the photocatalytic process, the potential of the photogenerated redox species is investigated using the band alignment or offset of the semiconductor material. The conduction band potential is calculated from the following equation,[55]

$$E_{CB} = \chi - E^e - 0.5E_g \qquad (3)$$

where of E_{CB} is the conduction band potential, χ is the electronegativity, E^e is potential of free electron on normal hydrogen energy (NHE) scale (4.50 eV)[55] and E_g is the apparent band gap energy of the doped material, while the valence band potential, E_{VB} is obtained from the sum of E_{CB} and E_g. The apparent band gap value of 2.67 eV is obtained from the apparent cut-off wavelength (465 nm). The electronegativity of the doped photoferroic is determined using the geometric mean electronegativity of the individual elements composing the material. The molar ratio is calculated from the percentage atomic concentration obtained by fitting the XPS data of 4 mol% Cr^{3+}-doped $BaTiO_3$, as summarized in Table 1. Only oxygen bonded to the lattice is considered. The results show that the photocatalytic process majorly proceeds through the formation of superoxide as the $E_{CB} \sim -0.885$ eV is higher in absolute value than the redox potential of $O_2/O_2^{-\cdot}$ species (-0.28 eV). Furthermore, as the valence band potential (1.785 eV) is lower than the potential of $OH^{\cdot}/OH^-$ (1.99 eV) and $OH^{\cdot}/H_2O$ (2.27 eV) redox couples, respectively, this indicates that the photo-oxidation of H_2O by holes to yield $OH^{\cdot}$ radical is unlikely. The charge transfer mechanism culminating from these band potentials is illustrated in Fig. 8d. Hence, this redox reaction cannot proceed even in the presence of large volume of photogenerated holes as they lack the expected oxidation potential to trigger the reaction. However, the involvement of $OH^{\cdot}$ as a supplementary radical through the dissociation of hydrogen peroxide (H_2O_2) generated from direct adduct of protonated superoxides is also possible and may not be ruled out. On the basis of internally generated spontaneous polarization, we remark that the stable configuration in the material leading to high energy barrier height as shown in Fig. 8d is affected. This culminates in the lowering of barrier height at the Helmholtz layer and consequently a slight tilt of the energy level due to the spontaneous polarization. Electrons and holes therefore gain sufficient energy to be transported across the surfaces in the polar material. Considering the samples with high concentration of chromium, the spontaneous polarization is weak as evidenced by Raman scattering results; thus an increased barrier height which does not favor sufficient transport of charge carriers across the interface. This probably contributes to the low degradation efficiency observed in these samples.

The kinetics of photodegradation depend on various competing processes such as absorption of photons and excitation of the photogenerated charge carriers, separation and transport of photoexcited charge carriers and surface redox

reactions.[56,57] The rate of photo-oxidation of methyl orange is examined by plotting $\ln(C_0/C_t)$ as a function of time, as shown in Fig. 8e. For all the samples, a linear behavior is observed, denoting a pseudo first-order kinetics for the liquid phase heterogeneous photocatalysis.[5] The slope corresponds to the observed apparent reaction rate constant, k_{obs} and a value of 0.0215 min^{-1} is estimated for the 4 mol% Cr^{3+}-doped $BaTiO_3$ nanoparticles, which is 2.7 times higher than that of the undoped sample (0.00798 min^{-1}).

For environmental applications, the photostability test is very important. Furthermore, this stability test excludes the possibility of "dye-sensitized" photoinduced oxidative degradation.[58,59] To investigate this, four series of controlled experimental reactions are conducted on the 4 mol% Cr^{3+}-doped $BaTiO_3$ sample, chosen for its high degradation efficiency. At the end of each reaction, the photocatalyst is recovered by: (i) decanting the used organic solution (ii) washing repeatedly in distilled water to remove adsorbed species of organic molecules, and (iii) drying in an oven at 80 °C. As observed in Fig. 8f, the degradation efficiency decreased by $\sim$6.6 ± 1.2% after the fourth cycle of simulated sunlight illumination. This deviation could be explained in terms of two factors: (i) instability, and (ii) slight loss of mass of the photocatalyst. Since the Raman features of the sample exist without apparent distortion (Fig. S5†), the latter is therefore expected to be the dominant factor.[60] This shows that the structural properties remain unchanged and thus Cr^{3+}-doped $BaTiO_3$ nanoparticles exhibit a good photocatalytic performance of up to the fourth cycle.

4 Conclusion

In summary, we describe the successful synthesis of photoferroic Cr^{3+}-doped $BaTiO_3$ nanoparticles by MWHT. The addition of mineralizer, H_2O_2 is used to control the process-related leakage current by scavenging the precipitated H^+/metal ions, making the materials suitable for photocatalytic applications due to the presence of screened surface charges. Both results of XRD and Raman scattering confirm a lattice distortion and a ferroelectric ordering in the non-centrosymmetric $BaTiO_3$ phase. The photoresponse of the host lattice is extended into the visible region up to $\lambda_{cut-off} = 480$ nm due to the d–d band transition of chromium. Moreover, XPS results show that the chromium exists in trivalent oxidation state while its presence slightly alters the binding energy of the host lattice.

We show that the photocatalytic activity, already enhanced with respect to that of $BaTiO_3$ due to the presence of the bulk photovoltaic effect, is further enhanced by the introduction of Cr up to 4 mol%. The latter is mainly attributed to an additional broad absorption band in the visible range. The best photoactivity is obtained with the 4 mol% Cr^{3+}-doped $BaTiO_3$, and remains stable up to the fourth cycle of irradiation. $O_2^{-\cdot}$ is perceived as the dominant active species from the in situ ROS capture experiments.

Conflicts of interest

There are no conflicts to declare.

Table 1 The electronegativity, atomic concentration as estimated from XPS and corresponding molar ratios for the 4 mol% Cr^{3+}-doped $BaTiO_3$ nanoparticles

Elements	Electronegativity, χ (eV)	At. conc. from XPS fitting (%)	Molar ratio
Ba	2.40 (ref. 61)	16.83	1.00
Ti	3.45 (ref. 61)	11.26	0.67
O	7.54 (ref. 61)	42.68	2.54
Cr	3.72 (ref. 61)	6.11	0.36

Acknowledgements

References

1 T. A. Kurniawan, L. Yanyan, T. Ouyang, A. B. Albadarin and G. Walker, *Mater. Sci. Semicond. Process.*, 2018, **73**, 42–50.

2 M. S. Mauter, I. Zucker, F. o. Perreault, J. R. Werber, J.-H. Kim and M. Elimelech, *Nat. Sustain.*, 2018, **1**, 166–175.

3 R. Su, Y. Shen, L. Li, D. Zhang, G. Yang, C. Gao and Y. Yang, *Small*, 2015, **11**, 202–207.

4 S. J. A. Moniz, S. A. Shevlin, D. J. Martin, Z.-X. Guo and J. Tang, *Energy Environ. Sci.*, 2015, **8**, 731–759.

5 O. Carp, C. L. Huisman and A. Reller, *Prog. Solid State Chem.*, 2004, **32**, 33–177.

6 J. Cao, Y. Ji, C. Tian and Z. Yi, *J. Alloys Compd.*, 2014, **615**, 243–248.

7 N. V. Dang, T. D. Thanh, L. V. Hong, V. D. Lam and T.-L. Phan, *J. Appl. Phys.*, 2011, **110**, 043914.

8 Y. Guo, T. Guo, J. Chen, J. Wei, L. Bai, X. Ye, Z. Ding, W. Xu and Z. Zhou, *Catal. Sci. Technol.*, 2018, **8**, 4108–4121.

9 J. Zhu, Z. Deng, F. Chen, J. Zhang, H. Chen, M. Anpo, J. Huang and L. Zhang, *Appl. Catal., B*, 2006, **62**, 329–335.

10 C. Srilakshmi, R. Saraf, V. Prashanth, G. M. Rao and C. Shivakumara, *Inorg. Chem.*, 2016, **55**, 4795–4805.

11 A. S. Bhalla, R. Guo and R. Roy, *Mater. Res. Innovations*, 2000, **4**, 3–26.

12 M. A. Pena and J. L. G. Fierro, *Chem. Rev.*, 2001, **101**, 1981–2017.

13 H.-W. Lee, S. Moon, C.-H. Choi, D. K. Kim and S. J. Kang, *J. Am. Ceram. Soc.*, 2012, **95**, 2429–2434.

14 V. P. Pavlovic, M. V. Nikolic, V. B. Pavlovic, J. Blanusa, S. Stevanovic, V. V. Mitic, M. Scepanovic, B. Vlahovic and M. Hoffman, *J. Am. Ceram. Soc.*, 2014, **97**, 601–608.

15 S. Nayak, B. Sahoo, T. K. Chaki and D. Khastgir, *RSC Adv.*, 2014, **4**, 1212–1224.

16 F. Li, M. Zeng, H. Yu, H. Xu and J. Li, *J. Mater. Sci.: Mater. Electron.*, 2015, **27**, 2836–2840.

17 K. T. Butler, J. M. Frost and A. Walsh, *Energy Environ. Sci.*, 2015, **8**, 838–848.

18 L. Zhang, O. P. Thakur, A. Feteira, G. M. Keith, A. G. Mould, D. C. Sinclair and A. R. West, *Appl. Phys. Lett.*, 2007, **90**, 142914.

19 S. Anwar, P. R. Sagdeo and N. P. Lalla, *J. Phys.: Condens. Matter*, 2006, **18**, 3455–3468.

20 B. Jiang, T. Grande and S. M. Selbach, *Chem. Mater.*, 2017, **29**, 4244–4252.

21 L. Gomathi Devi and P. M. Nithya, *Inorg. Chem. Front.*, 2018, **5**, 127–138.

22 R. Li, Q. Li, L. Zong, X. Wang and J. Yang, *Electrochim. Acta*, 2013, **91**, 30–35.

23 J. Rouxel and M. Toumoux, *Solid State Ionics*, 1996, **84**, 141–149.

24 R. J. Darton, S. S. Turner, J. Sloan, M. R. Lees and R. I. Walton, *Cryst. Growth Des.*, 2010, **10**, 3819–3823.

25 Y. Shiratori, C. Pithan, J. Dornseiffer and R. Waser, *J. Raman Spectrosc.*, 2007, **38**, 1288–1299.

26 H.-J. Freund and M. W. Roberts, *Surf. Sci. Rep.*, 1996, **25**, 225–273.

27 R. D. Shannon, *Acta Crystallogr., Sect. A: Cryst. Phys., Diffr., Theor. Gen. Crystallogr*, 1976, **32**, 751–767.

28 R. Moos, A. Gnudi and K. H. Härdtl, *J. Appl. Phys.*, 1995, **78**, 5042–5047.

29 O. M. Parkash, D. Kumar and C. C. Christopher, *J. Chem. Sci.*, 2003, **115**, 649–661.

30 G. M. Keith, M. J. Rampling, K. Sarma, N. M. Alford and D. C. Sinclair, *J. Eur. Ceram. Soc.*, 2004, **24**, 1721–1724.

31 G. M. Osoro, D. Bregiroux, M. P. Thi and F. Levassort, *Mater. Lett.*, 2016, **166**, 259–262.

32 V. M. Goldschmidt, *Naturwissenschaften*, 1926, **14**, 477–485.

33 G. K. Williamson and W. H. Hall, *Acta Metall.*, 1953, **1**, 22–31.

34 K. Brajesh, A. K. Kalyani and R. Ranjan, *Appl. Phys. Lett.*, 2015, **106**, 012907.

35 F. A. Rabuffetti and R. L. Brutchey, *J. Am. Chem. Soc.*, 2012, **134**, 9475–9487.

36 S. Wada, T. Suzuki and T. Noma, *Jpn. J. Appl. Phys.*, 1995, **34**, 5368–5379.

37 R. Asiaie, W. Zhu, S. A. Akbar and P. K. Dutta, *Chem. Mater.*, 1996, **8**, 226–234.

38 R.-j. Li, W.-x. Wei, J.-l. Hai, L.-x. Gao, Z.-w. Gao and Y.-y. Fan, *J. Alloys Compd.*, 2013, **574**, 212–216.

39 G. Pezzotti, *J. Appl. Phys.*, 2013, **113**, 211301.

40 Y.-S. Seo, J. S. Ahn and I.-K. Jeong, *J. Korean Phys. Soc.*, 2013, **62**, 749–755.

41 A. K. Sood, N. Chandrabhas, D. V. S. Muthu and A. Jayaraman, *Phys. Rev. B: Condens. Matter Mater. Phys.*, 1995, **51**, 8892–8896.

42 K.-R. Zhu, M.-S. Zhang, Q. Chen and Z. Yin, *Phys. Lett. A*, 2005, **340**, 220–227.

43 P. Pasierb, S. Komornicki, M. Rokita and M. Rekas, *J. Mol. Struct.*, 2001, **596**, 151–156.

44 S.-H. Shim, T. S. Duffy, R. Jeanloz, C.-S. Yoo and V. Iota, *Phys. Rev. B: Condens. Matter Mater. Phys.*, 2004, **69**, 144107–144112.

45 C. Peter, J. Kneer, K. Schmitt, A. Eberhardt and J. Wöllenstein, *Phys. Status Solidi A*, 2013, **210**, 403–407.

46 C. Miot, E. Husson, C. Proust, R. Erre and J. P. Coutures, *J. Eur. Ceram. Soc.*, 1998, **18**, 339–343.

47 S. Sodergren, H. Siegbahn, H. k. Rensmo, H. Lindstrom, A. Hagfeldt and S.-E. Lindquist, *J. Phys. Chem. B*, 1997, **101**, 3087–3090.

48 M. C. Biesinger, B. P. Payne, A. P. Grosvenor, L. W. M. Lau, A. R. Gerson and R. S. C. Smart, *Appl. Surf. Sci.*, 2011, **257**, 2717–2730.

49 I. Ikemoto, K. Ishii, S. Kinoshita, H. Kuroda, M. A. Alario Franco and J. M. Thomas, *J. Solid State Chem.*, 1976, **17**, 425–430.

50 H. T. Langhammer, T. Müller, R. Böttcher and H. P. Abicht, *J. Phys.: Condens. Matter*, 2008, **20**, 085206.

51 S. Eden, S. Kapphan, H. Hesse, V. Trepakov, V. Vikhnin, I. Gregora, L. Jastrabik and J. Seglins, *J. Phys.: Condens. Matter*, 1998, **10**, 10775–10786.

52 V. M. Fridkin, *Crystallogr. Rep.*, 2001, **46**, 654–658.

53 L. Yu, C. Wang, F. Chen, J. Zhang, Y. Ruan and J. Xu, *J. Mol. Catal. A: Chem.*, 2016, **411**, 1–8.

54 M. Z. Si, Y. P. Kang and Z. G. Zhang, *Appl. Surf. Sci.*, 2009, **255**, 6007–6010.

55 B. Chai, T. Peng, P. Zeng and X. Zhang, *Dalton Trans.*, 2012, **41**, 1179–1186.

56 M. Nakamura, S. Horiuchi, F. Kagawa, N. Ogawa, T. Kurumaji, Y. Tokura and M. Kawasaki, *Nat. Commun.*, 2017, **8**, 281.

57 C. Paillard, X. Bai, I. C. Infante, M. Guennou, G. Geneste, M. Alexe, J. Kreisel and B. Dkhil, *Adv. Mater.*, 2016, **28**, 5153–5168.

58 F. Niu, D. Chen, L. Qin, N. Zhang, J. Wang, Z. Chen and Y. Huang, *ChemCatChem*, 2015, **7**, 3279–3289.

59 B. Ohtani, *J. Photochem. Photobiol., C*, 2010, **11**, 157–178.

60 H. Huang, Y. He, X. Li, M. Li, C. Zeng, F. Dong, X. Du, T. Zhang and Y. Zhang, *J. Mater. Chem. A*, 2015, **3**, 24547–24556.

61 R. G. Pearson, *Inorg. Chem.*, 1988, **27**, 734–740.